

Article

High-Resolution Topographic Analyses of Mounds in Southern Acidalia Planitia, Mars: Implications for Possible Mud Volcanism in Submarine and Subaerial Environments

Ryodo Hemmi ^{1,*}  and Hideaki Miyamoto ^{1,2}

¹ The University Museum, The University of Tokyo, 7-3-1 Hongo, Bunkyo-ku, Tokyo 113-8656, Japan

² Department of Systems Innovation, School of Engineering, The University of Tokyo, 7-3-1 Hongo, Bunkyo-ku, Tokyo 113-8656, Japan; hm@sys.t.u-tokyo.ac.jp

* Correspondence: hemmi@seed.um.u-tokyo.ac.jp; Tel.: +81-3-3817-6842

Received: 29 March 2018; Accepted: 25 April 2018; Published: 27 April 2018



Abstract: A northern ocean of Mars is still debated and, if it existed, it may have accompanied valley networks and/or outflow channels, which may have led to the emplacement of a large amount of water to the northern lowlands during the Noachian and/or Hesperian times. However, it is unclear how and under what conditions (submarine or subaerial) geologic features such as mounds and giant polygons formed in the northern lowlands. The densely-distributed mounds in Chryse and Acidalia Planitia, >1000 km-wide basins of the northern plains, were suggested to be ancient mud volcanoes formed in an aqueous setting, which is controversial (i.e., mud vs. igneous and submarine vs. subaerial). However, these mounds have not been quantitatively well characterized, particularly with respect to their detailed topography. Here we generated forty digital elevation models (DEMs) with resolution of up to 1 m/pixel from High Resolution Imaging Science Experiment (HiRISE) stereo image pairs, and we accurately measured the morphometric parameters of ~1300 mounds within the southern part of the Acidalia basin. Their heights and diameters resulted in good accordance with those of mud and igneous volcanoes in submarine/subaerial settings on Earth. Maximum depths of their source reservoirs vary from ~30 to ~450 m for a subaqueous setting and from ~110 to ~860 m for a subaerial setting, both of which are consistent with fluid expulsion from the ~100–4500 m-thick flood deposits (Vastitas Borealis Formation, VBF). On the basis of the morphometric values, we estimated rheological properties of materials forming the mounds and found them consistent with a mud flow origin, which does not rule out an igneous origin. The conditions of possible submarine mud or igneous volcanoes may have harbored less hazardous environments for past life on Mars than those on an ocean-free surface.

Keywords: Mars; Acidalia Planitia; pitted mounds; HiRISE; digital elevation model; mud volcanism; submarine volcanism

1. Introduction

While liquid surface water is physically not stable under the current Martian climate, the former presence of a northern ocean (or northern oceans) has been proposed for the northern lowlands since either the Noachian [1,2] or the Hesperian [2–4]. There are two major views: (1) the valley networks, formed by the long-term hydrological cycle of a warm, wet climate during the Noachian, may have been associated with a persistent ocean [1]; (2) the Hesperian-aged cataclysmic floods, suggested by outflow channels debouching into the northern lowlands [5], may have left behind large amounts of water and sediments forming the northern ocean [6]. Observational evidence for their

marine sediments comes from the Vastitas Borealis Formation (VBF)—a roughly uniform sedimentary unit with an extent approximately equal to the northern lowlands [7–9]. The population of fresh craters superimposing the VBF suggests that it is the late Hesperian in age, and the surface roughness of underlying Hesperian-aged ridged plains indicates that the minimum average thickness of the VBF is ~100 m [9,10]. The lowest putative shoreline (Contact 2 or Deuteronilus shoreline [2–4]) encompasses most of the VBF and is much closer to the current equipotential surface of Mars at around –3760 m [6,11]. Ivanov et al. [12] conducted an extensive analysis of the shoreline and VBF and dated the Deuteronilus contact (VBF) to ~3.6 gigayears (Gyr) ago. Citron et al. [13] estimated the Arabia (the early Noachian period) and Deuteronilus (the early Hesperian period) ocean volumes of $\geq\sim 4.1 \times 10^7 \text{ km}^3$ and $\geq\sim 1.2 \times 10^7 \text{ km}^3$, respectively. Importantly, while various workers have hypothesized and tested these oceans and shorelines, a Noachian ocean does not contradict a Hesperian ocean and how long the northern oceans have persisted is uncertain.

The most prominent outflow channels are distributed around southern Chryse Planitia, and floods were estimated to have formed these circum-Chryse outflow channels and brought at least $6 \times 10^6 \text{ km}^3$ of water (assuming ~40% of sediment by volume) [14] or much more water (assuming lower sediment loads, such as 0.1% by volume of sediment, which is the case on Earth) [15] to the Chryse-Acidalia Embayment [16] (Figure 1). The VBF surfaces within the Acidalia basin have distinct textural features, such as polygonal fractures (or giant polygons) [17], mottled patterns (e.g., bright craters, cones, patches), and mounds with summit pits [6]. The puzzling issues are the conditions, timing, and processes that formed these mounds with this suite of characteristics.

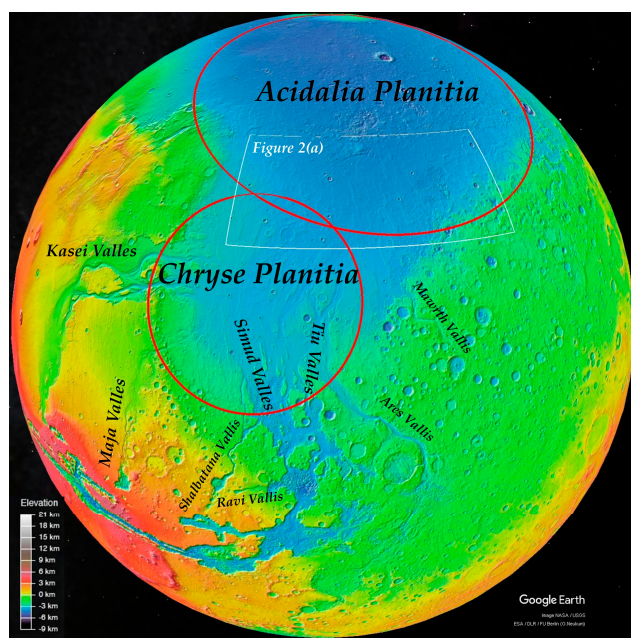


Figure 1. Mars globe overlaid by Mars Orbiter Laser Altimeter (MOLA) shaded relief/colorized elevation map (Image credit: Google Earth). Red circles show the approximate outlines of quasi circular depressions (buried impact basins, Chryse and Acidalia Planitia) [18]. Note that all of the named valleys represent circum-Chryse outflow channels.

A number of small-scale (10's of meters to a few kilometers wide), near-circular to irregular-shaped mounds with summit depressions (so-called “pitted mounds” [19–22]; also referred to as pitted cones, cratered cones, pitted domes [23–28]), have been commonly observed within the northern lowlands on Mars, such as Acidalia, Chryse, Isidis, Elysium, and Utopia Planitiae (e.g., [29]). The southern part of Acidalia Planitia (Figure 2) has crater retention ages between ~3.7 and ~3.4 Gyr [30–33] and its surface is geologically interpreted as either Late Hesperian or middle Amazonian lowland units [34]. More

than 18,000 mounds (>300 m diameter) were identified, and >40,000 mounds were estimated over southern Acidalia and northern Chryse regions [21,35,36].

Since pitted mounds in eastern Acidalia Planitia–Cydonia Mensae region were first recognized from Viking Orbiter images, terrestrial analog features of various origins have been proposed to explain their occurrence in the Acidalia basin, namely (1) rootless cones (or pseudocraters) formed by the emplacement of lava flows over wet ground and the subsequent explosions [37–41], (2) pyroclastic cones or cinder cones as a result of explosive eruptions and resultant depositions of pyroclastic materials [38,39,42–46], (3) secondary impact craters with inverted relief [38], (4) pingos caused by a volume increase of ground ice doming terrain surface [3,38,47], (5) tuff rings and tuff cones resulted from phreatomagmatic explosions [25,26], (6) spring mounds originated from evaporate deposits around spring vents [25], (7) mud volcanoes defined as surface manifestation of mud from depth [21,23,25,48–50], and a combination of two or more of the processes above.

Although none of these hypotheses have been proven decisively, the mud volcano hypothesis is considered to have one of the highest astrobiological potential among the above hypotheses. This is because terrestrial mud volcanoes commonly emit not only mud and water to the surface but biotic/abiotic, gaseous hydrocarbons (mostly methane), which, if formed on ancient Mars, is of great significance for interpreting regional magmatic and hydrothermal activity, distributions of clay minerals, present-day detection of atmospheric methane, their interaction with faults and fractures, and possible microbial activity [51]. Mud volcanoes on Earth occur both onshore and offshore, mostly along subduction zones (i.e., lateral tectonic compression zones) and/or in high sedimentation rate sites [52].

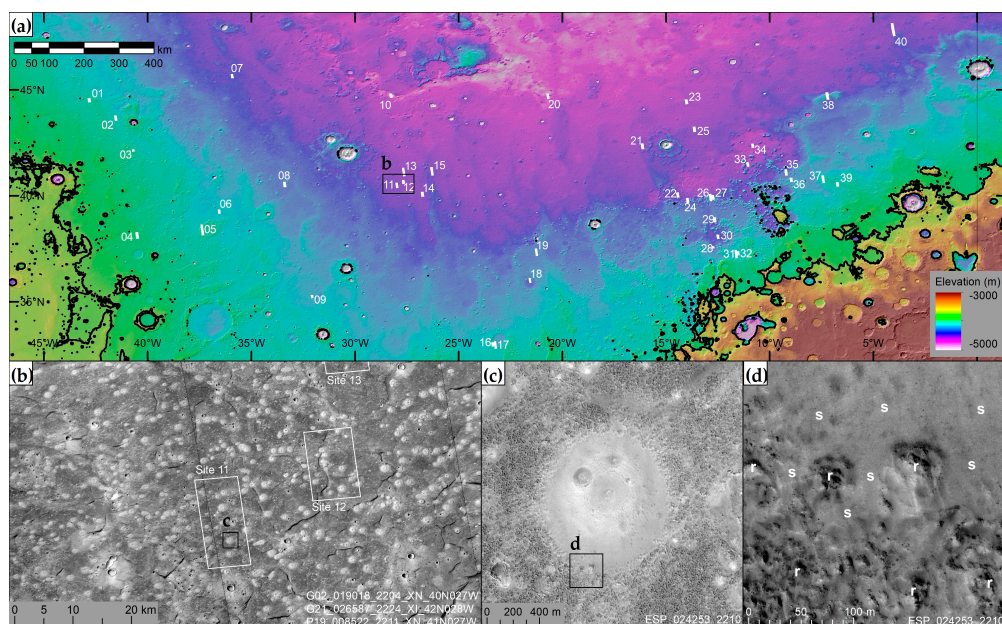


Figure 2. (a) MOLA gridded elevation overlain on MOLA hillshade background (128 pixels per degree) of northern Chryse–southern Acidalia region. The black lines are a –3760 m-contour approximating the Deuteronilus shoreline [2,11]. White-filled numbered rectangles represent the locations of digital elevation models (DEMs) generated in this study (Site 01 to 40, listed in Table 1). (b) Part of a mosaic of Mars Reconnaissance Orbiter (MRO) Context Camera (CTX) images [53], showing the central part of southern Acidalia Planitia. Pitted mounds appear as bright, circular features on the polygonally fractured terrain [17]. Sunlight illuminates the scene from the left. (c) A typical example of a pitted mound. Part of High Resolution Imaging Science Experiment (HiRISE) image ESP_024253_2210. Image credit: NASA/JPL/UA (University of Arizona). North is at the top. (d) Close-up view of the boundary between the mound and the surrounding plains in Figure 2c. Smooth mound materials (labeled as ‘s’) appear to overlie the surrounding terrain with relatively rough surfaces (labeled as ‘r’).

The previous observations in favor of the mud volcano interpretation are the results from geological data. For example, they are spatially related to other flow-related features [32,36]. They exhibit low thermal inertia relative to the surrounding plains measured from Mars Global Surveyor Thermal Emission Spectrometer (TES) [25] and Mars Odyssey Thermal Emission Imaging System (THEMIS) [54] data, which is consistent with finer-grained materials covering the mound surfaces, and the geologic setting of the Chryse-Acidalia Embayment is a depositional basin [16]. High Resolution Imaging Science Experiment (HiRISE) cameras onboard the Mars Reconnaissance Orbiter (MRO) revealed that many of the mounds in southern Acidalia have bright, smooth surface materials outwardly extending from their peripheries over the rough surrounding plains (e.g., Figure 2c,d; [21]), which suggests the expansion of mound materials occurred on the pre-existing surface. Several mounds show distinct flow features emanating from them (e.g., Supplementary Figure S8; [21]), indicating that the materials behaved as fluids during the mound formation. Other common morphologies include summit and flank pits (Figure 2c), concentric crest structures, surrounding moats, smooth surface textures, which are consistent with the mud volcanic features. However, the biggest problem is that all of the above observations do not rule out alternative interpretations (e.g., igneous volcanoes).

It should be noted that most of the mounds are located more than a few hundred meters below the Deuteronilus shoreline level (~3760 m; Figure 2a [2,11]). On the basis of a close spatial relationship of giant polygons and pitted mounds (Figure 2b; mounds located just inside polygonal troughs in Supplementary Figures S12 and S13) and its analogy to that of kilometer-sized polygons and terrestrial mud volcanoes in marine settings on Earth [55,56], Oehler and Allen [55] hypothesized that their co-occurrence in the Chryse-Acidalia area may have resulted from fluid expulsion processes of sediment-laden flood water. They suggested that late Hesperian deposition from outflow floods caused a rapid deposition of unconsolidated fine-grained sediments in an aqueous basin, which subsequently developed polygonal fracturing. They also characterized the geometries of submarine mounds and polygons on Earth by using high-resolution 3-D seismic data.

Those of the Martian counterparts were, however, not examined because of lacking high-resolution topographic data. The resolution of the global digital elevation models (DEMs) created based on Mars Global Surveyor (MGS) Mars Orbiter Laser Altimeter (MOLA) is 128 pixels/degree or ~463 m/pixel. Each spot (~168 m in diameter) of MOLA observation is separated about 300 m along track [57], which is insufficient to determine the shape of these mounds precisely. Thus, although geometric characterization of the Acidalia mounds are critical for quantitatively assessing how they were formed (e.g., modeling of materials for the mounds), the topographic studies of the mounds were limited to Viking image-based (low-resolution), photoclinometric measurements of about 400 mounds (>400 m wide) with unspecified locations in Acidalia and Chryse Planitia [23,45].

In this study we extracted high-resolution DEMs from HiRISE stereo images of pitted mounds over the entire southern part of Acidalia Planitia (Figure 2a; ~32°–49° N, ~317°–357° E). We then analyzed the relationship between their heights (a few meters to tens of meters) and diameters (tens of meters to a few kilometers) for almost 1300 mounds (Section 3), then tested consistency with a submarine (or subaerial) mud volcano hypothesis by estimating mud reservoir depths and by making first-order estimates of the rheological parameters of fluid flows (Section 4).

Table 1. List of DEMs derived from HiRISE image pairs at each site.

Site	HiRISE Stereo Pair Image 1 ID	HiRISE Stereo Pair Image 2 ID	Center Longitude (°E) ¹	Center Latitude (°N) ¹	Resolution (m/Pixel)
01	ESP_019612_2250	ESP_025203_2250	317.1833	44.5086	1.0
02	ESP_024227_2240	ESP_024359_2240	318.4598	43.6649	1.0
03	PSP_002233_2225	PSP_002866_2225	319.2983	42.1368	1.0
04	PSP_009063_2185	PSP_009485_2185	319.4896	38.1269	1.0
05	ESP_037255_2185	ESP_037954_2185	322.6237	38.3876	2.0

Table 1. Cont.

Site	HiRISE Stereo Pair Image 1 ID	HiRISE Stereo Pair Image 2 ID	Center Longitude ($^{\circ}$ E) ¹	Center Latitude ($^{\circ}$ N) ¹	Resolution (m/Pixel)
06	PSP_002457_2195	PSP_002536_2195	323.4403	39.2529	1.0
07	ESP_024728_2260	ESP_027207_2260	324.0668	45.6430	1.0
08	ESP_014258_2210	ESP_022974_2210	326.6019	40.5313	2.0
09	ESP_034499_2155	ESP_034934_2155	327.9202	35.2393	1.0
10	ESP_018517_2250	ESP_018649_2250	331.7310	44.7243	1.0
11	ESP_024253_2210	ESP_024530_2210	332.0099	40.4877	1.0
12	ESP_018728_2210	ESP_019018_2210	332.3311	40.6531	1.0
13	ESP_027919_2215	ESP_028064_2215	332.3398	41.1169	2.0
14	ESP_017950_2205	ESP_018583_2205	333.2518	40.0696	1.0
15	ESP_026732_2215	ESP_027431_2215	333.7049	41.1558	2.0
16	ESP_021642_2135	ESP_021919_2135	336.6412	32.9827	1.0
17	ESP_026244_2130	ESP_026521_2130	336.7620	32.9493	1.0
18	ESP_025822_2165	ESP_027101_2165	338.4331	35.9987	1.0
19	ESP_034248_2175	ESP_034314_2175	338.7390	37.3332	2.0
20	ESP_028934_2250	ESP_037716_2250	339.2974	44.6937	2.0
21	PSP_009906_2225	PSP_010196_2225	343.8611	42.3290	1.0
22	PSP_007770_2205	PSP_007981_2205	345.5654	40.0352	1.0
23	ESP_017132_2250	ESP_017633_2250	345.9836	44.4325	2.0
24	PSP_005700_2200	ESP_011818_2200	346.0364	39.7757	1.0
25	ESP_018134_2235	ESP_018411_2235	346.3654	43.1340	1.0
26	ESP_032850_2200	ESP_033641_2200	347.1340	39.9110	1.0
27	PSP_009708_2205	PSP_009985_2205	347.2636	39.9283	1.0
28	PSP_002232_2180	PSP_002377_2180	347.2682	37.5626	1.0
29	ESP_019334_2190	ESP_028380_2190	347.3528	38.8651	2.0
30	ESP_016011_2185	ESP_016499_2185	347.5016	38.0586	1.0
31	ESP_026204_2175	ESP_034762_2175	348.3709	37.2445	1.0
32	ESP_034485_2175	ESP_035698_2175	348.4768	37.2845	2.0
33	ESP_027892_2220	ESP_028182_2220	348.9297	41.4773	2.0
34	ESP_028670_2225	ESP_037465_2225	349.1695	42.3576	2.0
35	PSP_009642_2215	PSP_010143_2215	350.7889	41.1003	1.0
36	PSP_008574_2210	PSP_009497_2210	351.0352	40.7468	1.0
37	ESP_025439_2210	ESP_025518_2210	352.5708	40.7737	1.0
38	ESP_016301_2250	ESP_016578_2250	352.7775	44.7067	1.0
39	ESP_023316_2210	ESP_023606_2210	353.2687	40.5359	2.0
40	ESP_025663_2280	ESP_026362_2280	355.9435	47.8408	4.0

¹ The values of center longitude and latitude of each DEM were used as the central meridian and standard parallel, respectively when DEMs are mapped to an equirectangular projection.

2. Data and Methods

We extracted forty high-resolution DEMs (1.0, 2.0, or 4.0 m/post) and corresponding orthoimages for the areas of pitted mounds in the southern part of Acidalia Planitia (e.g., Figure 3a; see also Table 1 and Supplementary Figures S1 to S40). In generating stereo image DEMs, we followed, with minor differences, the workflows of [22]. First, we performed radiometric calibration, bundle adjustment, shifting, mosaicking, and map projection of the Experimental Data Records (EDRs; ten or nine HiRISE RED-filtered raw image files) of HiRISE stereo pairs [58,59] using the US Geological Survey's Integrated Software for Imagers and Spectrometers (ISIS) 3.4.6 [60–62]. We used HiRISE image pairs that have ideal camera pointing (moderate convergence angle), good image quality (no severe atmospheric hazes or imaging errors), and 1×1 , 2×2 or 4×4 pixel binning as stereo pairs. For the application of bundle adjustment to each pair of HiRISE images, we collected hundreds of image control points between image pairs and three or more ground control points from Mars Express's High Resolution Stereo Camera (HRSC) nadir-channel images at spatial resolutions of 12.5 to 50.0 m/pixel [63]. These HRSC images are map-projected beforehand onto THEMIS geodetically controlled mosaic [64] of the southern Acidalia region using the ISIS software. All raw and calibrated image data are available in National Aeronautics and Space Administration (NASA) Planetary Data System (PDS). We then used a control network of these points to update camera pointing and spacecraft position information of each HiRISE stereo pair with the ISIS's module for bundle adjustment, jigsaw [65].

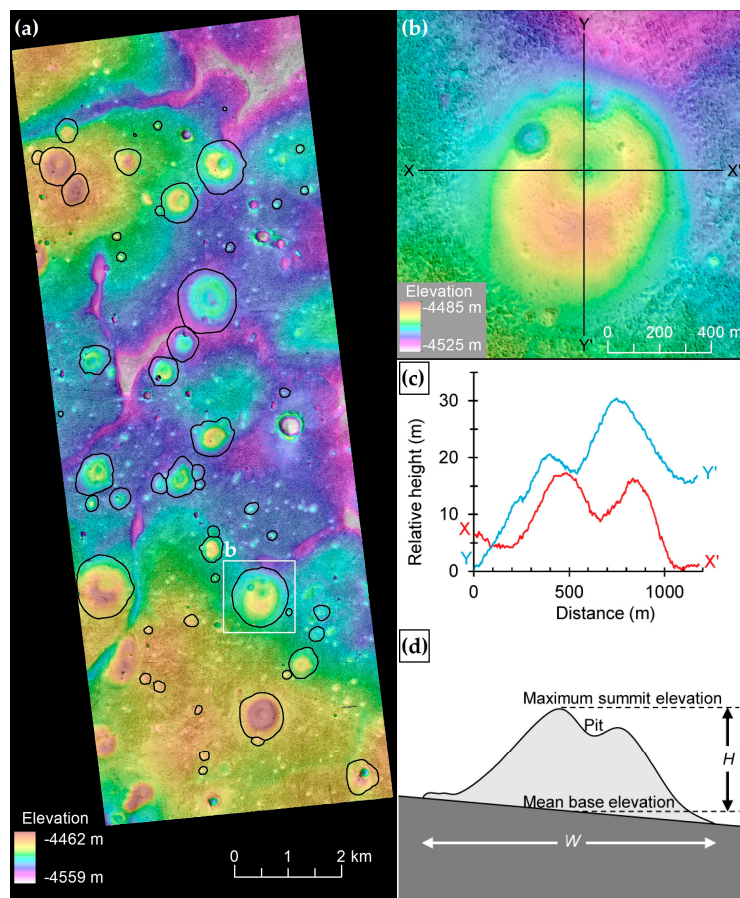


Figure 3. (a) Example of a HiRISE-derived DEM (1 m/pix) overlain on a contrast-enhanced orthoimage (1 m/pix), equivalent to Supplementary Figure S11. The solid black lines outline the periphery of each pitted mound that are manually delineated for the measurements of the basal area and average base elevation. (b) Close-up indicated in Figure 3a. This mound is equivalent to Mound 12 of Site 11. The black lines (X–X' and Y–Y') indicate the location of the topographic profile shown in Figure 2c. North is at the top. (c) Topographic profiles across a pitted mound (as shown in Figure 3b). Vertical exaggeration is about 30 times. (d) Schematic cross-section of a pitted mound and morphologic parameters measured in this study. H : maximum mound height, W : mound basal width. The vertical scale is highly exaggerated.

NASA's Ames Stereo Pipeline (ASP) 2.4.2 [66–68] software was used to perform integer image correlation (match correlation window size of 21×21 pixels), sub-pixel refinement (window size of 25×25 pixels), disparity filtering, stereo triangulation, and generation of a gridded DEM. To minimize vertical differences between DEMs and the global Mars Global Surveyor (MGS) Mars Orbiter Laser Altimeter (MOLA [57]) elevation model (128 pixels/degree or ~ 463 m/pixel), the mean value of height differences between each DEM and resampled (1, 2, or 4 m/pixels) MOLA data are subtracted from each DEM, using the Geospatial Data Abstraction Library (GDAL) 2.0.2 and Environmental Systems Research Institute (ESRI) ArcGIS Desktop ArcMap 10.2.2 software.

The resultant vertical accuracies are expected to be around several tens of centimeters for ASP-derived DEMs. This value is comparable to ASP-derived (non-bundle adjusted) DEMs and BAE Systems' SOCET SET-derived (bundle-adjusted) DEMs (so-called "HiRISE Digital Terrain Model (DTM)"; <https://www.uahirise.org/dtm/>) with vertical accuracy of ~ 20 cm [58,59] (published by the HiRISE Science Team and the USGS), root mean square errors of the discrepancies are better than

0.50 m [69,70]. On the basis of viewing geometry and ground pixel scale [71,72], we also calculated the vertical accuracy values, assuming 0.2-pixel matching error [58,59],

$$\text{Vertical Accuracy} = 0.2 * \text{GSD} / (\text{Parallax}/\text{Height}) \quad (1)$$

$$\text{Parallax}/\text{Height} = \sqrt{(PX_1 - PX_2)^2 + (PY_1 - PY_2)^2} \quad (2)$$

$$PX = -\tan(EA) \cos(SGA) \quad (3)$$

$$PY = \tan(EA) \sin(SGA), \quad (4)$$

where GSD is the ground sample distance which in this case is equivalent to the larger ground pixel size between the two images (mostly spatial resolution of more oblique images), the subscripts 1 and 2 refer to the two images, PX is a parallax in the X direction, PY is a parallax in the Y direction, EA is an emission angle, and SGA is a sub-spacecraft ground azimuth, which can be extracted by using the ISIS campt application. The resultant values are limited to a range of ~0.1 to 0.6 meters (Table 2).

Table 2. Expected vertical accuracy values for each DEMs.

Site	Image 1		Image 2		Parallax/Height	GSD (m/Pixel)	Vertical Accuracy (m)
	EA (°)	SGA (°)	EA (°)	SGA (°)			
01	3.55	269.47	18.68	265.90	0.28	0.32	0.23
02	25.27	80.30	2.82	271.27	0.52	0.33	0.13
03	6.26	267.21	21.23	265.80	0.28	0.32	0.23
04	7.09	266.57	19.73	265.52	0.23	0.31	0.27
05	5.67	79.01	10.51	265.81	0.28	0.60	0.42
06	30.24	80.45	2.38	73.91	0.54	0.34	0.13
07	7.86	266.68	9.62	80.11	0.31	0.31	0.20
08	7.53	79.97	28.51	80.45	0.41	0.67	0.33
09	16.34	265.43	14.11	80.94	0.54	0.31	0.11
10	2.39	74.13	27.51	266.40	0.56	0.34	0.12
11	2.59	74.54	17.39	265.70	0.36	0.31	0.18
12	2.14	273.24	18.54	80.81	0.37	0.32	0.17
13	20.08	265.81	5.15	267.90	0.28	0.63	0.46
14	5.69	267.40	21.18	265.75	0.29	0.32	0.22
15	4.80	268.29	22.78	265.90	0.34	0.32	0.19
16	0.38	332.34	25.59	265.43	0.48	0.32	0.14
17	3.58	77.33	20.16	265.33	0.43	0.31	0.15
18	5.71	267.33	18.95	81.03	0.44	0.31	0.14
19	2.82	75.36	14.32	265.63	0.30	0.61	0.40
20	7.92	79.78	16.37	265.90	0.43	0.63	0.29
21	8.49	266.32	15.96	80.71	0.43	0.31	0.14
22	7.87	80.06	6.81	266.77	0.26	0.30	0.24
23	7.31	266.79	6.18	79.33	0.24	0.61	0.51
24	0.37	1.48	26.64	265.88	0.50	0.33	0.13
25	19.47	80.65	1.81	275.29	0.38	0.32	0.17
26	7.27	266.60	23.91	80.65	0.57	0.32	0.11
27	15.37	80.82	6.92	266.73	0.40	0.31	0.16
28	6.03	267.20	7.31	80.03	0.23	0.30	0.26
29	0.37	1.10	14.40	265.70	0.26	0.31	0.24
30	28.06	80.68	2.64	75.17	0.49	0.33	0.14
31	1.78	70.93	29.39	265.87	0.59	0.34	0.11
32	2.51	272.02	22.18	80.86	0.45	0.64	0.28
33	17.06	265.77	13.76	80.65	0.55	0.62	0.22
34	6.93	266.97	4.87	78.35	0.21	0.61	0.59
35	1.40	278.59	18.18	80.76	0.35	0.32	0.18
36	4.73	78.50	14.77	265.67	0.35	0.31	0.18
37	1.88	71.29	29.91	80.29	0.54	0.34	0.13
38	4.36	268.48	22.76	266.10	0.34	0.33	0.19
39	1.80	71.28	21.25	80.78	0.36	0.64	0.36
40	4.70	78.03	20.74	266.19	0.46	0.65	0.28

We calculated both the height H and basal width W for manually delineated individual mounds (e.g., Figure 3; Supplementary Figures S1 to S40) in each DEM. To provide accurate measurements of

each pitted mound, mounds lacking a summit pit, degraded mounds, fully coalesced mounds forming complex topographies, and mounds including invalid DEM pixels have been carefully excluded from our measurements. H is defined as the difference between the maximum summit elevation and average base elevation [73,74] (Figure 3d), and W is the diameter of a circle having the same area as that of an outlined mound area [74,75].

Taking into account the vertical accuracy and post spacing for each DEM, as well as the minor uncertainties in morphometric measurements ascribed to the manual delineations of each mound (Supplementary Figures S1 to S40), maximum errors in height and width are expected to be 0.6 m and 2.0 m for DEMs at 1.0 m/pixel, 1.2 m and 4.0 m for DEMs at 2.0 m/pixel, and 2.4 m and 8.0 m for DEMs at 4.0 m/pixel. To test the validity of our measurements, we have compared H values of 21 mounds in Site 09 extracted from in our DEM (Supplementary Figure S9) with those derived using a HiRISE DTM (Supplementary Figure S41) and confirmed the discrepancies of both values in these two DEMs are within at most 0.6 m (Table 3).

Table 3. Comparisons of morphometric parameters of 21 measured mounds extracted from both our ASP-derived DEM (Figure S9) and a SOCET SET-derived DEM (Figure S41).

Mound	H (m)		Difference (m)
	Our DEM	Published DEM	
1	26.2	26.4	-0.2
2	21.6	21.9	-0.3
3	8.9	9	-0.1
4	11.8	12	-0.2
5	13.1	13.4	-0.3
6	21.1	21.2	-0.1
7	22.5	22.6	-0.1
8	20.5	20.8	-0.3
9	17.4	18	-0.6
10	12.2	12.4	-0.2
11	19.1	19.2	-0.1
12	8.1	8.2	-0.1
13	12.3	12.5	-0.2
14	17.2	17.6	-0.4
15	12.2	12.4	-0.2
16	21	21.4	-0.4
17	19.9	20.1	-0.2
18	13.5	13.9	-0.4
19	4.1	4.4	-0.3
20	10.2	10.2	0
21	14.7	14.7	0

3. Results

Morphometric measurements were performed for 1297 pitted mounds within southern Acidalia Planitia (see Figure 4 and Table S1). The basal diameters W range from 39 to 1406 m, with a mean and median of 367 and 327 m, respectively, and a standard deviation (std. dev.) of 226 m. The mound heights H are in the range of 1.1–69.5 m with a mean (median) and a std. dev. of 15.2 (12.6) \pm 10.8 m. The data indicate no substantial dependence on latitude, longitude, or elevation. Previous studies, such as the photoclinometric analysis of over 400 pitted mounds within Cydonia Mensae, part of the Acidalia basin, and Chryse Planitia [23,45] and mound heights derived from three MOLA track data in Acidalia [25], are fairly comparable to our results. The exception being that a 3D photogrammetric analysis of HiRISE stereo pairs involving two pitted mounds by Oehler and Allen [21] (the same two mounds in Site 03) resulted in heights of up to 180 m, which are an order of magnitude larger than those of our results (30.8 and 31.6 m in height). This difference is hard to interpret because the past analysis was not described in detail. The ranges of H and W values and height-to-diameter ratios (H/W) of terrestrial and Martian analogous features for comparison with the mounds measured in this study are summarized in Figure 4 and Table 4.

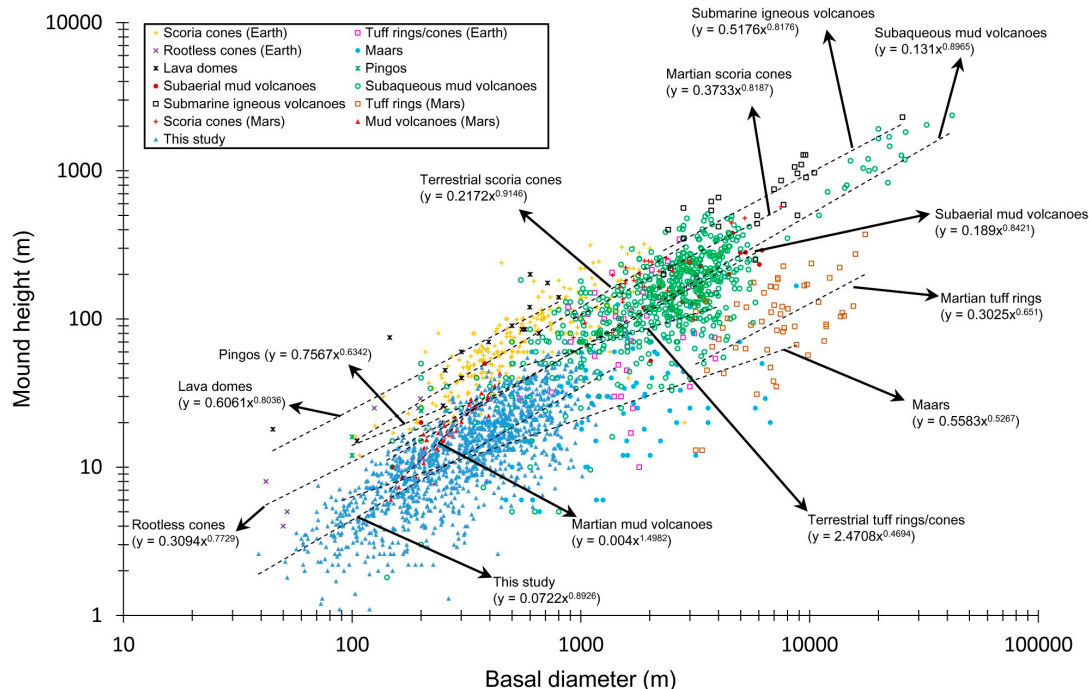


Figure 4. Log-log plot showing the measured maximum height (H) versus basal diameter (W) for 1297 pitted mounds in southern Acidalia Planitia (see also Table S1) and analogous features on Earth and Mars [22,76]. The dashed lines represent the best-fit power regression.

Table 4. A summary of morphometric parameters of the mounds shown in Figure 4.

Feature Type	N	H Range (Average)	W Range (Average)	H/W Range (Average)
Earth				
Scoria cones	241	12–320 m (85 m)	104–2843 m (640 m)	0.007–0.53 (0.137)
Tuff rings/cones	43	10–345 m (104 m)	541–3900 m (1915 m)	0.006–0.15 (0.059)
Rootless cones	10	4–29 m (17 m)	42–355 m (174 m)	0.063–0.20 (0.111)
Maars	77	4–167 m (34 m)	91–8750 m (1900 m)	0.003–0.10 (0.023)
Lava domes	16	15–200 m (83 m)	45–800 m (424 m)	0.104–0.51 (0.213)
Pingos	4	12–24 m (19 m)	100–260 m (165 m)	0.09–0.16 (0.12)
Subaerial mud volcanoes	21	10–380 m (154 m)	150–6200 m (2872 m)	0.026–0.13 (0.061)
Subaqueous mud volcanoes	619	1.8–2365 m (188 m)	142–42000 m (3026 m)	0.006–0.33 (0.067)
Submarine igneous volcanoes	24	200–2300 m (738 m)	2300–25500 m (7010 m)	0.043–0.199 (0.113)
Mars				
Scoria cones	28	75–573 m (218 m)	928–7500 m (2347 m)	0.03–0.14 (0.097)
Tuff rings/cones	52	13–372 m (117 m)	3179–17535 m (8045 m)	0.004–0.037 (0.016)
Mud volcanoes (Terra Sirenum)	50	6–43 m (17.8 m)	147–442 m (265 m)	0.034–0.10 (0.065)
This study	1297	1.1–69.5 m (15.2 m)	39–1406 m (367 m)	0.005–0.13 (0.043)

4. Discussion

4.1. Comparison of Morphometric Parameters among Possible Origins

As shown in Figure 4 and Table 4, some features on Earth and Mars show morphometric parameters similar to those of the mounds measured in this study and the others do not, which may give some clues as to what types of features are less or more likely origins of the mounds in Acidalia. Rootless cones (Earth), maars (Earth), pingos (Earth), subaerial/subaqueous mud volcanoes (Earth), and Martian mud volcanoes (Terra Sirenum) have the ranges of all three parameters relatively consistent with those of the mounds measured in this study. Regarding the ranges of the H values, submarine igneous volcanoes and Martian scoria cones are about one order of magnitude larger than the mounds measured in this study. As for the ranges of the W values, submarine igneous volcanoes, Martian scoria cones, and Martian tuff rings/cones show one or more orders of magnitude larger values than those measured in this study. With regard to the H/W ratio ranges (and average values), terrestrial lava domes show values more than two times higher than those of the other features. It should be noted that different environments (gravity, atmosphere, rock types, compositions, etc.) may have affected the mound formation processes. As suggested by Brož et al. [77], the thin atmosphere and low gravity on Mars are expected to cause far-reaching ballistic emplacement of scoria, creating wider and lower volcanic cones than those on Earth. This does not affect the interpretation that submarine igneous volcanoes, scoria cones and tuff rings/cones on Mars are less likely origins because Martian counterparts are much larger than the Acidalia mounds. However, Wilson and Head [46] proposed that the low gravity of Mars causes cooling-limited lava flows to be ~6 times longer on Earth, which decreases their H/W ratios significantly. That is why lava domes cannot be ruled out in the context of the morphometric parameters. Relative to igneous volcanism, mud volcanism is generally not such an explosive or high temperature process. Hence, the morphometric parameters of mud volcanoes on Mars are expected to be similar to those of terrestrial mud volcanoes, which are consistent with Table 4. However, another potentially serious caveat of the above discussion is that, after formation of the mounds, erosional or alteration processes could have deformed their topography to date and the observed topography can be quite different from the original one, which complicates the comparisons to newly formed analogs on Earth. If the mud volcanoes formed in a subaqueous setting (or under an ocean) 3.6 Gyr ago, several possibilities of significantly altering their topography should be considered: e.g., submarine landslide, wave erosion, outflow channel floods, periglacial deformation, wind erosion, multiple eruptions, dust cover, etc. Estimating to what extent each of these processes contribute to the deformation is hard to determine due to large uncertainties. Therefore, although the comparison of morphometric parameters provides helpful information for distinguishing the possible origins, we cannot fully rely on the results and the interpretation of this analysis.

4.2. Depths of the Sources in Subaqueous or Subaerial Conditions

Oehler and Allen [55] suggested that part of Chryse-Acialia Planitia hosted oceans and associated marine sediments to cause fluid expulsion producing submarine mud volcanoes during late Hesperian [2,78]. However, subaerial mud volcanism has not been well discussed and ruled out. Here we will assess under which conditions (submarine, subaerial, or both) fluid expulsion caused mud eruptions by using a simple mud eruption model.

In order to operate, mud volcanism would have required subsurface mud reservoirs prior to mud eruptions, and they should have been composed of water-enriched, fine-grained sediments. On Earth, the upwelling of fluidized mud primarily requires the presence of conduits connecting the reservoirs and the surface, and a bulk density inversion between mud reservoirs and overlying materials. As for the former, on Mars, polygonal fractures (or giant polygons) underlying the mounds appear to have acted as the conduits [55,56]. If the other processes that increase the pore pressure of mud reservoirs, such as horizontal compressional forces and additional groundwater, are negligible, an isostatic compensation model to relate the height of a mud volcano (H) to the depth of a putative

mud source (D) can be developed (Figure 5). The balance between the weight of the sediment column with ambient materials (air/water) and that of the mud volcano column constrains the depth to the top of the mud source:

$$D = H(\rho_m - \rho_a)/(\rho_s - \rho_m) \quad (5)$$

where ρ_m is the bulk density of mud, ρ_s is the bulk density of the surface layers which overlie the mud sources, ρ_a is the bulk density of ambient materials during the eruption (1.0 kg/m³ for liquid water and 0.020 kg/m³ for air). This buoyancy-driven model has been applied to igneous volcanoes [79–81] and submarine mud volcanoes [82,83] on Earth for the first-order analyses. Although variations in gas and fluid content can create large density differences in the mud, we assume $\rho_m = 1400\text{--}2100\text{ kg/m}^3$ to be a plausible range of bulk mud densities because it is comparable to that measured at most submarine and subaerial mud volcanoes on Earth (the density values of 1400 kg/m³ and 2100 kg/m³ correspond to those of clast-free, mousse-like silty clays and clast-bearing mud breccia, respectively) [83–88].

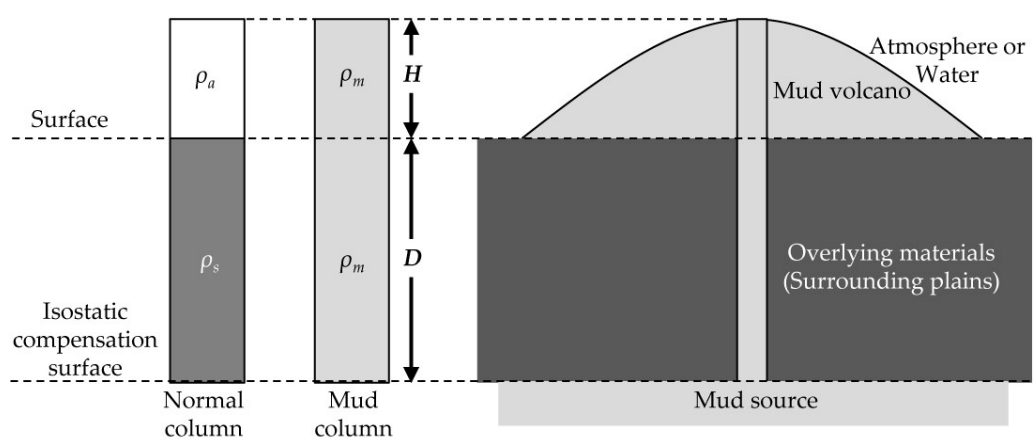


Figure 5. Schematic diagram of a simple buoyancy model of mud volcano formation [83]. D : isostatic compensation depth to the top of the mud source (i.e., thickness of overburden above mud source), ρ_m : bulk density of erupted mud through conduit, ρ_s : bulk density of overlying materials, ρ_a : bulk density of ambient materials.

The bulk density of surface materials (ρ_s) overlying mud source reservoirs within the southern Acidalia region is not readily determined because northern lowlands may consist of stratigraphic layers with different compositions (e.g., aeolian, ejecta, volcanic ash, ice-rich material), and their porosities could be a function of depth [2]. Thus, we assume that a real part of bulk dielectric permittivity (ϵ') is a function of the depth-averaged bulk density (ρ_b) of the dry geologic materials [89]:

$$\epsilon' = 1.96^{\rho_b} \quad (6)$$

Using a value of ϵ' associated with the Vastitas Borealis interior unit [27] (~4.6 [90]), which includes the southern Acidalia region to a depth of 60–80 m [91], we can obtain $\rho_s = 2270\text{ kg/m}^3$, which is also consistent with bulk densities of modeled country rock with a porosity of 25% at depths of 1 to 2 km [46]. If a subaqueous setting existed during mud eruptions, then source depths D are estimated at 0.5–32.0 m (mean = 7.0 m) to 7.1–449.7 m (mean = 98.3 m) for $\rho_m = 1400$ to 2100 kg/m^3 . Alternatively, considering a subaerial setting, we calculate $D = 1.8\text{--}111.8\text{ m}$ (mean = 24.4 m) to 13.6–858.5 m (mean = 187.7 m) for $\rho_m = 1400$ to 2100 kg/m^3 . While the thickness of the circum-Chryse outflow sediments forming the present VBF surface is uncertain, its thickness estimates range from ~100 m [9] to ~4500 m [92] (summarized in the discussion of [55]). Therefore, in either case, the estimated depths of the mud columns can be explained by fluid expulsions from the at most ~4.5 km-thick VBF sediments. Due to the above reasons, we conclude that, if the Acidalia mounds have been formed by the fluid expulsion

from the late Hesperian-aged flood deposits, either subaqueous or subaerial setting may have existed during the mud eruption.

4.3. Testing the Rheology of Fluid Flows

As previously proposed by Oehler and Allen [21], appearances of smooth surface flows at their peripheries (e.g., Supplementary Figure S8), together with upward doming topographic profiles (Figure 3c), strongly suggest (1) they were formed by emplacement of the fluids with finite yield strengths and plastic viscosities and (2) they are formed through single events (or the final shapes represent the bulk rheological properties throughout their formational events). However, the proposed mud flows creating the mounds have not been quantitatively examined in the context of rheological parameters. In this section, we test this idea by applying their morphometric parameters to fluid flow models and comparing the resultant rheological parameters with those measured at terrestrial mud volcanoes.

A slurry (a high concentration of cohesive clay particles in water) are commonly approximated as Bingham plastic fluids [93]. When a Bingham fluid slowly spreads over a plane it retains a convex-upward geometry in cross-section with its maximum height proportional to the square root of the yield strength multiplied by its basal width (i.e., a parabolic cross-section) [81,94–97]. Assuming that each singular flow of a uniform Bingham fluid formed each of the mounds, and the thickness of the center of this fluid can be approximately equal to the mound height H regardless of a summit depression, the yield strength τ_y of materials forming each mound can be described as,

$$\tau_y = (\rho g H^2) / W \quad (7)$$

where ρ is the bulk density of a fluid and g is the surface gravity on present Mars ($\sim 3.71 \text{ m/s}^2$). Here we take $\rho = 2000 \text{ kg/m}^3$, which was chosen as a typical value within the value range used in Section 4.1.

Substituting the H and W values measured from the mounds into Equation (7), we obtain that the Bingham yield strengths for the fluids were in the range of $4.8 \times 10^1 \text{ Pa}$ to $4.4 \times 10^4 \text{ Pa}$ with a mean (median) value of $5.6 (3.8) \times 10^3 \text{ Pa}$, as listed in Supplementary Table S2. These yield strength estimates are of similar magnitude to those of samples from submarine mud volcanoes (10^3 – 10^4 Pa [83,98]) and subaerial mud volcanoes (10^1 – 10^5 Pa [87,99]). Thus, pitted mounds may be formed by a mixture of liquid water and loosely cemented, fine-grained sediments (e.g., mud slurries), which may explain the observed high albedo and low thermal inertia rather than the surrounding plains [25,54]. Cross-sectional profiles of pitted mounds in Acidalia (e.g., Figure 3c) are similar in morphology to those of typical mud volcanoes on Earth [100], which can also support the hypothesized mud flows.

If this modeling is acceptable, mud viscosity, a significant factor to constrain flow rate, can be roughly estimated. Both yield strengths (τ_y) and viscosities (η) in fine-grained slurries are known to be functions of volumetric sediment concentrations (C_v),

$$\tau_y = \alpha_1 \exp(C_v \beta_1), \quad (8)$$

$$\eta = \alpha_2 \exp(C_v \beta_2), \quad (9)$$

where α_1 , α_2 , β_1 , and β_2 are empirical constants that vary with the ratio of silt-and-clay ($<63 \mu\text{m}$ grain size) to sand ($>63 \mu\text{m}$ grain size) in slurries [101,102]. Inserting the expression for C_v from Equation (8) into Equation (9), we obtain an equation regarding the viscosity as:

$$\eta = \alpha_2 (\tau_y / \alpha_1)^{\beta_2 / \beta_1}. \quad (10)$$

The four empirical constants in Equation (10) were assumed to be comparable to the values of the slurries which have a silt-and-clay to sand ratio of 11:1 ($\alpha_1 = 3.79 \times 10^{-6} \text{ Pa}$, $\alpha_2 = 6.76 \times 10^{-17} \text{ Pa s}$,

$\beta_1 = 33.07$, $\beta_2 = 73.54$ [102]), because several mud samples from different terrestrial mud volcanoes are composed of silt and clay with 1–25% sand [85,87,99,103]. By substituting the results from Equation (6) into Equation (9), the resulting viscosities (η) range from 4.2×10^{-1} Pa s to 1.6×10^6 Pa s with a mean (median) value of 4.3×10^4 Pa s (6.9×10^3 Pa s) (Supplementary Table S2). These values are consistent with the mud viscosities of several mud volcano samples (0.8–1.5 Pa s [86], 100– 10^3 Pa s [99], 10^5 Pa s [104], and 10^6 Pa s [88]), which come from different bulk densities and/or water contents at different times in different places on Earth. Perhaps a variation of the estimated η values may also represent the temporal and spatial variability of bulk physical properties of muds erupted from different reservoirs on ancient Mars.

4.4. Geological Context of the Mounds in Acidalia Basin

The morphology, topography, morphometry, and modeled rheological properties of the mounds, as stated above, are consistent with both a mud volcano and an igneous volcano origins; though, low or moderate regional gravity data of GSFC Gravity Model (GGM1025) [105,106], relative to Tharsis and Elysium regions, (see Figure 14 of [21]) strongly suggest the absence of high-density igneous bodies (i.e., magma sources) below the Acidalia surface. Moreover, according to Salvatore and Christensen [54], the analyses of THEMIS-derived thermal inertia map revealed that the materials forming the Acidalia mounds and the VBF marginal unit [27] clearly exhibit lower thermal inertia relative to the surrounding terrain (the VBF interior unit [27]), which indicates that the Acidalia mounds were composed of fine-grained sedimentary materials, produced by the expulsion of mud from the shallow subsurface. As a consequence, in the context of non-volcanic geological setting and thermophysical characteristics, we propose that a mud volcano hypothesis is favored over a magmatic hypothesis for the case of the mounds in Acidalia basin.

5. Conclusions

We created high-resolution digital elevation models, measured the accurate morphometry of nearly 1300 mounds in the Acidalia basin of Martian northern lowlands, and quantitatively assessed the possibility of subaerial/subaqueous mud volcanism by using simple mound formation models. In either case, maximum depth estimates of source reservoirs (less than ~860 or ~450 m) are consistent with mud eruptions caused by fluid expulsions of the at most ~4.5-km-thick Hesperian flood deposits (the present-day VBF surface). In a submarine setting, the Noachian-aged valley networks or the Hesperian-aged outflow channels may have provided a vast amount of water and sediments forming the northern ocean, and during this period, a rapid sedimentation could have triggered fluid expulsion processes creating mud volcanoes (e.g., scenario A of [29]). Alternatively, subsequent sublimation of the surface water could have provided ocean-free surfaces during the late Hesperian or the Amazonian period. Perhaps circum-Chryse outflow events were episodically active, which may have never produced the northern oceans. This subaerial setting may have experienced impact-induced seismic shaking and associated fluidization of subsurface reservoirs may have caused mud volcanism (e.g., scenario E of [29]).

Observational evidence, morphometric measurements, and the estimated rheological estimates of mound-forming materials altogether strongly suggest that the mounds were formed by mud volcanism, which does rule out igneous volcanism. However, on the basis of the absence of a subsurface magma source and the mounds having lower thermal inertia relative to the surrounding plains, we propose the mud volcanism is more plausible hypothesis than igneous volcanism. Similar mud volcanism may have occurred in other areas within northern lowlands, such as Utopia and Isidis basins, where both circular mounds and fractures over the Hesperian-aged VBF(-like) surfaces have been observed [32,107–109]. Unlike the potential hazards of terrestrial mud volcano fields in onshore (e.g., LUSI mud volcano, East Java, Indonesia, triggered by drilling operations [110]) and offshore settings [111], the potential oceans and associated mud volcanoes on ancient Mars may have provided the inventory of a significant amount of liquid water and dissolved gasses, which is also the case for submarine igneous volcanism

(e.g., a seamount of Izu–Bonin Arc [112]). In a submarine setting, ocean(s) may have provided more habitable environments for a relatively long period of time than those in a subaerial setting because a large standing body of water possibly protects life against various threats, such as cosmic ray irradiation [113] and UV radiation [114]. Because terrestrial mud volcanic provinces generally provide favorable environments of methane emission and microbial life [115], sediments beneath mud volcano features on Mars may preserve extant aquifers and/or gas hydrate systems, and perhaps traces of past life, which can be one of the most suitable sites for future Mars landing missions.

Supplementary Materials: The following are available online at <http://www.mdpi.com/2076-3263/8/5/152/s1>, Figures S1–S40: Color-coded, high-resolution DEM draped over a contrast-enhanced grayscale orthoimage for Site 01 to Site 40, Figure S41: a published HiRISE DTM used for the comparison of morphometric parameters of mounds, Table S1: Morphometric parameters of the 1297 pitted mounds at 40 study sites, Table S2: Estimated yield strengths and reservoir depths for all the mounds.

Author Contributions: R.H. and H.M. conceived and designed research; R.H. analyzed data; R.H. and H.M. wrote the paper.

Acknowledgments: This work was supported by JSPS KAKENHI Grant Numbers JP16K13890 and JP17H02953. We appreciate the TOKYO DOME CORPORATION for their great support of the Space Museum TeNQ and the branch of Space Exploration Education and Discovery (SEED), the University Museum, the University of Tokyo. We thank HiRISE science team for producing publicly available, high-resolution image datasets. We also appreciate the developers of USGS Integrated Software for Imagers and Spectrometers for enabling us to handle Mars image datasets. We are grateful to NASA Ames Stereo Pipeline developers for creating open source software used to generate DEMs. Elpitha Howington-Kraus was very helpful answering questions about generation of SOCET SET-derived DEMs and theoretical estimates of vertical accuracy of DEMs. We acknowledge Zachary Morrato, Ross Beyer, Oleg Alexandrov, and Trent Hare for their helpful comments on the extraction of DEMs and relevant GIS processing and Reid Parsons for helpful corrections. The authors also would like to thank three anonymous reviewers for greatly improving the manuscript.

Conflicts of Interest: The authors declare no conflict of interest.

References

1. Baker, V.R.; Strom, R.G.; Gulick, V.C.; Kargel, J.S.; Komatsu, G.; Kale, V.S. Ancient oceans, ice sheets and the hydrological cycle on mars. *Nature* **1991**, *352*, 589. [[CrossRef](#)]
2. Clifford, S.M.; Parker, T.J. The evolution of the martian hydrosphere: Implications for the fate of a primordial ocean and the current state of the northern plains. *Icarus* **2001**, *154*, 40–79. [[CrossRef](#)]
3. Parker, T.J.; Gorsline, D.S.; Saunders, R.S.; Pieri, D.C.; Schneeberger, D.M. Coastal geomorphology of the martian northern plains. *J. Geophys. Res. Planets* **1993**, *98*, 11061–11078. [[CrossRef](#)]
4. Parker, T.J.; Stephen Saunders, R.; Schneeberger, D.M. Transitional morphology in west deuteronilus mensae, mars: Implications for modification of the lowland/upland boundary. *Icarus* **1989**, *82*, 111–145. [[CrossRef](#)]
5. Baker, V.R.; Milton, D.J. Erosion by catastrophic floods on mars and earth. *Icarus* **1974**, *23*, 27–41. [[CrossRef](#)]
6. Carr, M.H. *The Surface of Mars*; Cambridge University Press: Cambridge, UK, 2007.
7. Scott, D.H.; Tanaka, K.L. *Geologic Map of the Western Equatorial Region of Mars*; USGS: Reston, VA, USA, 1986.
8. Tanaka, K.L.; Scott, D.H. *Geologic Map of the Polar Regions of Mars*; USGS: Reston, VA, USA, 1987.
9. Kreslavsky, M.A.; Head, J.W. Fate of outflow channel effluents in the northern lowlands of mars: The vastitas borealis formation as a sublimation residue from frozen ponded bodies of water. *J. Geophys. Res. Planets* **2002**, *107*, 4-1–4-25. [[CrossRef](#)]
10. Head, J.W.; Kreslavsky, M.A.; Pratt, S. Northern lowlands of mars: Evidence for widespread volcanic flooding and tectonic deformation in the hesperian period. *J. Geophys. Res. Planets* **2002**, *107*, 3-1–3-29. [[CrossRef](#)]
11. Head, J.W.; Hiesinger, H.; Ivanov, M.A.; Kreslavsky, M.A.; Pratt, S.; Thomson, B.J. Possible ancient oceans on mars: Evidence from mars orbiter laser altimeter data. *Science* **1999**, *286*, 2134–2137. [[CrossRef](#)] [[PubMed](#)]
12. Ivanov, M.A.; Erkeling, G.; Hiesinger, H.; Bernhardt, H.; Reiss, D. Topography of the deuteronilus contact on mars: Evidence for an ancient water/mud ocean and long-wavelength topographic readjustments. *Planet. Space Sci.* **2017**, *144*, 49–70. [[CrossRef](#)]
13. Citron, R.I.; Manga, M.; Hemingway, D.J. Timing of oceans on mars from shoreline deformation. *Nature* **2018**, *555*, 643–646. [[CrossRef](#)] [[PubMed](#)]
14. Carr, M.H. *Water on Mars*; Oxford University Press: New York, NY, USA, 1996.

15. Turbet, M.; Forget, F.; Head, J.W.; Wordsworth, R. 3D modelling of the climatic impact of outflow channel formation events on early mars. *Icarus* **2017**, *288*, 10–36. [[CrossRef](#)]
16. Oehler, D.Z.; Allen, C.C. Focusing the search for biosignatures on mars: Facies prediction with an example from acidalia planitia. In *Sedimentary Geology of Mars*; Grotzinger, J.P., Milliken, R.E., Eds.; SEPM (Society for Sedimentary Geology): Tulsa, OK, USA, 2012.
17. Lucchitta, B.K.; Ferguson, H.M.; Summers, C. Sedimentary deposits in the northern lowland plains, mars. *J. Geophys. Res. Solid Earth* **1986**, *91*, E166–E174. [[CrossRef](#)]
18. Frey, H. Ages of very large impact basins on mars: Implications for the late heavy bombardment in the inner solar system. *Geophys. Res. Lett.* **2008**, *35*, L13203. [[CrossRef](#)]
19. Martínez-Alonso, S.; Mellon, M.T.; Banks, M.E.; Keszthelyi, L.P.; McEwen, A.S.; Team, T.H. Evidence of volcanic and glacial activity in chryse and acidalia planitiae, mars. *Icarus* **2011**, *212*, 597–621. [[CrossRef](#)]
20. Ramsdale, J.D.; Balme, M.R.; Conway, S.J.; Gallagher, C.; van Gasselt, S.A.; Hauber, E.; Orgel, C.; Séjourné, A.; Skinner, J.A.; Costard, F.; et al. Grid-based mapping: A method for rapidly determining the spatial distributions of small features over very large areas. *Planet. Space Sci.* **2017**, *140*, 49–61. [[CrossRef](#)]
21. Oehler, D.Z.; Allen, C.C. Evidence for pervasive mud volcanism in acidalia planitia, mars. *Icarus* **2010**, *208*, 636–657. [[CrossRef](#)]
22. Hemmi, R.; Miyamoto, H. Distribution, morphology, and morphometry of circular mounds in the elongated basin of northern terra sirenum, mars. *Prog. Earth Planet. Sci.* **2017**, *4*, 26. [[CrossRef](#)]
23. Tanaka, K.L. Sedimentary history and mass flow structures of chryse and acidalia planitiae, mars. *J. Geophys. Res. Planets* **1997**, *102*, 4131–4149. [[CrossRef](#)]
24. Carr, M.H.; Head, J.W. Oceans on mars: An assessment of the observational evidence and possible fate. *J. Geophys. Res. Planets* **2003**, *108*. [[CrossRef](#)]
25. Farrand, W.H.; Gaddis, L.R.; Keszthelyi, L. Pitted cones and domes on mars: Observations in acidalia planitia and cydonia mensae using moc, themis, and tes data. *J. Geophys. Res. Planets* **2005**, *110*, E05005. [[CrossRef](#)]
26. McGill, G.E. *Geologic Map of Cydonia Mensae—Southern Acidalia Planitia, Mars, Quadrangles MTM 40007, 40012, 40017, 45007, 45012, and 45017*; U.S. Geological Survey Geologic Investigations Series I-2811; USGS: Reston, VA, USA, 2005.
27. Tanaka, K.L.; Skinner, J.A.; Hare, T.M. Geologic map of the northern plains of mars. In *U.S. Geological Survey Scientific Investigations Map 2888*; USGS: Reston, VA, USA, 2005.
28. Dundas, C.M.; Keszthelyi, L.P.; McEwen, A.S.; Team, H. Initial hirise observations of cratered cone groups on mars. In Proceedings of the 38th Lunar and Planetary Science Conference, League City, TX, USA, 12–16 March 2007; p. 2116.
29. Skinner, J.A.; Mazzini, A. Martian mud volcanism: Terrestrial analogs and implications for formation scenarios. *Mar. Pet. Geol.* **2009**, *26*, 1866–1878. [[CrossRef](#)]
30. Werner, S.C.; Tanaka, K.L.; Skinner, J.A. Mars: The evolutionary history of the northern lowlands based on crater counting and geologic mapping. *Planet. Space Sci.* **2011**, *59*, 1143–1165. [[CrossRef](#)]
31. Platz, T.; Michael, G.; Tanaka, K.L.; Skinner, J.A.; Fortezzo, C.M. Crater-based dating of geological units on mars: Methods and application for the new global geological map. *Icarus* **2013**, *225*, 806–827. [[CrossRef](#)]
32. Ivanov, M.A.; Hiesinger, H.; Erkeling, G.; Reiss, D. Evidence for large reservoirs of water/mud in utopia and acidalia planitiae on mars. *Icarus* **2015**, *248*, 383–391. [[CrossRef](#)]
33. Warner, N.H.; Gupta, S.; Calef, F.; Grindrod, P.; Boll, N.; Goddard, K. Minimum effective area for high resolution crater counting of martian terrains. *Icarus* **2015**, *245*, 198–240. [[CrossRef](#)]
34. Tanaka, K.L.; Skinner, J.A.J.; Dohm, J.M.; Irwin Iii, R.P.; Kolb, E.J.; Fortezzo, C.M.; Platz, T.; Michael, G.G.; Hare, T. Geologic map of mars, scale 1:20,000,000. In *U.S. Geological Survey Scientific Investigations Map 3292*; USGS: Reston, VA, USA, 2014.
35. Amador, E.S.; Allen, C.C.; Oehler, D.Z. Regional mapping and spectral analysis of mounds in acidalia planitia, mars. In Proceedings of the 41st Lunar and Planetary Science Conference, The Woodlands, TX, USA, 1–5 March 2010; p. 1037.
36. Skinner, J.A. Constraining the origin of pitted cones in chryse and acidalia planitiae, mars, based on their statistical distributions and marginal relationships. In Proceedings of the 43rd Lunar and Planetary Science Conference, The Woodlands, TX, USA, 19–23 March 2012; p. 2905.
37. Frey, H.; Lowry, B.L.; Chase, S.A. Pseudocraters on mars. *J. Geophys. Res. Solid Earth* **1979**, *84*, 8075–8086. [[CrossRef](#)]

38. Lucchitta, B.K. Mars and earth: Comparison of cold-climate features. *Icarus* **1981**, *45*, 264–303. [[CrossRef](#)]
39. Frey, H.; Jarosewich, M. Subkilometer martian volcanoes: Properties and possible terrestrial analogs. *J. Geophys. Res. Solid Earth* **1982**, *87*, 9867–9879. [[CrossRef](#)]
40. Carr, M.H. Mars: A water-rich planet? *Icarus* **1986**, *68*, 187–216. [[CrossRef](#)]
41. Fagents, S.A.; Lanagan, P.; Greeley, R. Rootless cones on mars: A consequence of lava-ground ice interaction. *Geol. Soc. Lond. Spec. Publ.* **2002**, *202*, 295–317. [[CrossRef](#)]
42. Ann Hodges, C.; Moore, H.J. The subglacial birth of olympus mons and its aureoles. *J. Geophys. Res. Solid Earth* **1979**, *84*, 8061–8074. [[CrossRef](#)]
43. Wood, C.A. Monogenetic volcanoes of the terrestrial planets. In Proceedings of the 10th Lunar and Planetary Science Conference, Houston, TX, USA, 19–23 March 1979; pp. 2815–2840.
44. Greeley, R.; Spudis, P.D. Volcanism on mars. *Rev. Geophys.* **1981**, *19*, 13–41. [[CrossRef](#)]
45. Davis, P.A.; Tanaka, K.L. Morphometries and possible terrestrial analogs of small martian volcanoes. In Proceedings of the 25th Lunar and Planetary Science Conference, Houston, TX, USA, 14–18 March 1994; p. 317.
46. Wilson, L.; Head, J.W. Mars: Review and analysis of volcanic eruption theory and relationships to observed landforms. *Rev. Geophys.* **1994**, *32*, 221–263. [[CrossRef](#)]
47. Rossbacher, L.A.; Judson, S. Ground ice on mars: Inventory, distribution, and resulting landforms. *Icarus* **1981**, *45*, 39–59. [[CrossRef](#)]
48. Komar, P.D. Mud volcanoes on mars. In *Reports of Planetary Geology and Geophysics Program, 1990*; NASA: Washington, DC, USA, 1991; pp. 539–541.
49. Keszthelyi, L.P.; Jaeger, W.L.; Dundas, C.M.; Martínez-Alonso, S.; McEwen, A.S.; Milazzo, M.P. Hydrovolcanic features on mars: Preliminary observations from the first mars year of hirise imaging. *Icarus* **2010**, *205*, 211–229. [[CrossRef](#)]
50. McGowan, E. Spatial distribution of putative water related features in southern acidalia/cydonia mensae, mars. *Icarus* **2009**, *202*, 78–89. [[CrossRef](#)]
51. Oehler, D.Z.; Etiope, G. Methane seepage on mars: Where to look and why. *Astrobiology* **2017**, *17*, 1233–1264. [[CrossRef](#)] [[PubMed](#)]
52. Milkov, A.V. Worldwide distribution of submarine mud volcanoes and associated gas hydrates. *Mar. Geol.* **2000**, *167*, 29–42. [[CrossRef](#)]
53. Malin, M.C.; Bell, J.F.; Cantor, B.A.; Caplinger, M.A.; Calvin, W.M.; Clancy, R.T.; Edgett, K.S.; Edwards, L.; Haberle, R.M.; James, P.B.; et al. Context camera investigation on board the mars reconnaissance orbiter. *J. Geophys. Res. Planets* **2007**, *112*, E05S04. [[CrossRef](#)]
54. Salvatore, M.R.; Christensen, P.R. On the origin of the vastitas borealis formation in chryse and acidalia planitia, mars. *J. Geophys. Res. Planets* **2014**, *119*, 2437–2456. [[CrossRef](#)]
55. Oehler, D.Z.; Allen, C.C. Giant polygons and mounds in the lowlands of mars: Signatures of an ancient ocean? *Astrobiology* **2012**, *12*, 601–615. [[CrossRef](#)] [[PubMed](#)]
56. Allen, C.C.; Oehler, D.Z.; Etiope, G.; Van Rensbergen, P.; Baciu, C.; Feyzullayev, A.; Martinelli, G.; Tanaka, K.; Van Rooij, D. Fluid expulsion in terrestrial sedimentary basins: A process providing potential analogs for giant polygons and mounds in the martian lowlands. *Icarus* **2013**, *224*, 424–432. [[CrossRef](#)]
57. Smith, D.E.; Zuber, M.T.; Frey, H.V.; Garvin, J.B.; Head, J.W.; Muhleman, D.O.; Pettengill, G.H.; Phillips, R.J.; Solomon, S.C.; Zwally, H.J. Mars orbiter laser altimeter: Experiment summary after the first year of global mapping of mars. *J. Geophys. Res. Planets* **2001**, *106*, 23689–23722. [[CrossRef](#)]
58. McEwen, A.S.; Eliason, E.M.; Bergstrom, J.W.; Bridges, N.T.; Hansen, C.J.; Delamere, W.A.; Grant, J.A.; Gulick, V.C.; Herkenhoff, K.E.; Keszthelyi, L.; et al. Mars reconnaissance orbiter’s high resolution imaging science experiment (hirise). *J. Geophys. Res. Planets* **2007**, *112*, E05S02. [[CrossRef](#)]

59. Kirk, R.L.; Howington-Kraus, E.; Rosiek, M.R.; Anderson, J.A.; Archinal, B.A.; Becker, K.J.; Cook, D.A.; Galuszka, D.M.; Geissler, P.E.; Hare, T.M.; et al. Ultrahigh resolution topographic mapping of mars with mro hirise stereo images: Meter-scale slopes of candidate phoenix landing sites. *J. Geophys. Res. Planets* **2008**, *113*, E00A24. [[CrossRef](#)]
60. Gaddis, L.; Anderson, J.; Becker, K.; Becker, T.; Cook, D.; Edwards, K.; Eliason, E.; Hare, T.; Kieffer, H.; Lee, E.M. An overview of the integrated software for imaging spectrometers (ISIS). In Proceedings of the 28th Lunar and Planetary Science Conference, Houston, TX, USA, 17–21 March 1997; p. 1226.
61. Torson, J.M.; Becker, K.J. ISIS—A software architecture for processing planetary images. In Proceedings of the 28th Lunar and Planetary Science Conference, Houston, TX, USA, 17–21 March 1997; p. 1219.
62. Anderson, J.A.; Sides, S.C.; Soltesz, D.L.; Sucharski, T.L.; Becker, K.J. Modernization of the integrated software for imagers and spectrometers. In Proceedings of the 35th Lunar and Planetary Science Conference, League City, TX, USA, 15–19 March 2004; p. 2039.
63. Neukum, G.; Jaumann, R. Hrsc: The high resolution stereo camera of mars express. In *Mars Express: The Scientific Payload*; ESA: Noordwijk, The Netherlands, 2004; Volume SP-1240, pp. 17–35.
64. Fergason, R.L.; Lee, E.M.; Weller, L. Themis geodetically controlled mosaics of mars. In Proceedings of the 44th Lunar and Planetary Science Conference, The Woodlands, TX, USA, 18–22 March 2013; p. 1642.
65. Edmundson, K.L.; Cook, D.A.; Thomas, O.H.; Archinal, B.A.; Kirk, R.L. Jigsaw: The ISIS3 bundle adjustment for extraterrestrial photogrammetry. *ISPRS Ann. Photogramm. Remote Sens. Spat. Inf. Sci.* **2012**, *I-4*, 203–208. [[CrossRef](#)]
66. Broxton, M.J.; Edwards, L.J. The ames stereo pipeline: Automated 3d surface reconstruction from orbital imagery. In Proceedings of the 39th Lunar and Planetary Science Conference, League City, TX, USA, 10–14 March 2008; p. 2419.
67. Moratto, Z.M.; Broxton, M.J.; Beyer, R.A.; Lundy, M.; Husmann, K. Ames stereo pipeline, nasa’s open source automated stereogrammetry software. In Proceedings of the 41st Lunar and Planetary Science Conference, The Woodlands, TX, USA, 1–5 March 2010; p. 2364.
68. Shean, D.E.; Alexandrov, O.; Moratto, Z.M.; Smith, B.E.; Joughin, I.R.; Porter, C.; Morin, P. An automated, open-source pipeline for mass production of digital elevation models (dems) from very-high-resolution commercial stereo satellite imagery. *ISPRS J. Photogramm. Remote Sens.* **2016**, *116*, 101–117. [[CrossRef](#)]
69. Re, C.; Roncella, R.; Forlani, G.; Cremonese, G.; Naletto, G. Evaluation of area-based image matching applied to dtm generation with hirise images. *ISPRS Ann. Photogramm. Remote Sens. Spat. Inf. Sci.* **2012**, *I-4*, 209–214. [[CrossRef](#)]
70. Watters, W.A.; Geiger, L.M.; Fendrock, M.; Gibson, R. Morphometry of small recent impact craters on mars: Size and terrain dependence, short-term modification. *J. Geophys. Res. Planets* **2015**, *120*, 226–254. [[CrossRef](#)]
71. Becker, K.J.; Archinal, B.A.; Hare, T.H.; Kirk, R.L.; Howington-Kraus, E.; Robinson, M.S.; Rosiek, M.R. Criteria for automated identification of stereo image pairs. In Proceedings of the 46th Lunar and Planetary Science Conference, The Woodlands, TX, USA, 16–20 March 2015; Volume 46, p. 2703.
72. Beddingfield, C.B.; Burr, D.M.; Emery, J.P. Fault geometries on uranus’ satellite miranda: Implications for internal structure and heat flow. *Icarus* **2015**, *247*, 35–52. [[CrossRef](#)]
73. Settle, M. The structure and emplacement of cinder cone fields. *Am. J. Sci.* **1979**, *279*, 1089–1107. [[CrossRef](#)]
74. Kervyn, M.; Ernst, G.G.J.; Carracedo, J.C.; Jacobs, P. Geomorphometric variability of “monogenetic” volcanic cones: Evidence from mauna kea, lanzarote and experimental cones. *Geomorphology* **2012**, *136*, 59–75. [[CrossRef](#)]
75. Favalli, M.; Karátson, D.; Mazzarini, F.; Pareschi, M.T.; Boschi, E. Morphometry of scoria cones located on a volcano flank: A case study from mt. Etna (Italy), based on high-resolution lidar data. *J. Volcanol. Geotherm. Res.* **2009**, *186*, 320–330. [[CrossRef](#)]
76. Batiza, R.; Vanko, D. Volcanic development of small oceanic central volcanoes on the flanks of the east pacific rise inferred from narrow-beam echo-sounder surveys. *Mar. Geol.* **1983**, *54*, 53–90. [[CrossRef](#)]
77. Brož, P.; Čadek, O.; Hauber, E.; Rossi, A.P. Scoria cones on mars: Detailed investigation of morphometry based on high-resolution digital elevation models. *J. Geophys. Res. Planets* **2015**, *120*, 1512–1527. [[CrossRef](#)]
78. Jakosky, B.M.; Phillips, R.J. Mars’ volatile and climate history. *Nature* **2001**, *412*, 237–244. [[CrossRef](#)] [[PubMed](#)]
79. Vogt, P.R. Volcano height and plate thickness. *Earth Planet. Sci. Lett.* **1974**, *23*, 337–348. [[CrossRef](#)]
80. Smith, D.K.; Cann, J.R. Building the crust at the mid-Atlantic ridge. *Nature* **1993**, *365*, 707–715. [[CrossRef](#)]
81. Melosh, H.J. *Planetary Surface Processes*; Cambridge University Press: Cambridge, UK, 2011.

82. Henry, P.; Le Pichon, X.; Lallement, S.; Foucher, J.-P.; Westbrook, G.; Hobart, M. Mud volcano field seaward of the barbados accretionary complex: A deep-towed side scan sonar survey. *J. Geophys. Res. Solid Earth* **1990**, *95*, 8917–8929. [[CrossRef](#)]
83. Murton, B.J.; Biggs, J. Numerical modelling of mud volcanoes and their flows using constraints from the gulf of Cadiz. *Mar. Geol.* **2003**, *195*, 223–236. [[CrossRef](#)]
84. Volgin, A.V.; Woodside, J.M. Sidescan sonar images of mud volcanoes from the mediterranean ridge: Possible causes of variations in backscatter intensity. *Mar. Geol.* **1996**, *132*, 39–53. [[CrossRef](#)]
85. Lance, S.; Henry, P.; Le Pichon, X.; Lallement, S.; Chamley, H.; Rostek, F.; Faugères, J.-C.; Gonthier, E.; Olu, K. Submersible study of mud volcanoes seaward of the barbados accretionary wedge: Sedimentology, structure and rheology. *Mar. Geol.* **1998**, *145*, 255–292. [[CrossRef](#)]
86. Rifai, R. *Spatial Modelling and Risk Assessment of Sidoarjo Mud Volcanic Flow*; Gadjah Mada University: Yogyakarta, Indonesia, 2008.
87. Kopf, A.; Stegmann, S.; Delisle, G.; Panahi, B.; Aliyev, C.S.; Guliyev, I. In situ cone penetration tests at the active dashgil mud volcano, Azerbaijan: Evidence for excess fluid pressure, updoming, and possible future violent eruption. *Mar. Pet. Geol.* **2009**, *26*, 1716–1723. [[CrossRef](#)]
88. Kopf, A.; Behrmann, J.H. Extrusion dynamics of mud volcanoes on the mediterranean ridge accretionary complex. *Geol. Soc. Lond. Spec. Publ.* **1999**, *174*, 169. [[CrossRef](#)]
89. Ulaby, F.T.; Bengal, T.; East, J.; Dobson, M.C.; Garvin, J.; Evans, D. *Microwave Dielectric Spectrum of Rocks*; 23817-1-T; University of Michigan: Ann Arbor, MI, USA, 1988.
90. Mouginot, J.; Pommerol, A.; Beck, P.; Kofman, W.; Clifford, S.M. Dielectric map of the Martian northern hemisphere and the nature of plain filling materials. *Geophys. Res. Lett.* **2012**, *39*. [[CrossRef](#)]
91. Mouginot, J.; Pommerol, A.; Kofman, W.; Beck, P.; Schmitt, B.; Herique, A.; Grima, C.; Safaeinili, A.; Plaut, J.J. The 3–5 MHz global reflectivity map of mars by marsis/mars express: Implications for the current inventory of subsurface H₂O. *Icarus* **2010**, *210*, 612–625. [[CrossRef](#)]
92. Zuber, M.T.; Solomon, S.C.; Phillips, R.J.; Smith, D.E.; Tyler, G.L.; Aharonson, O.; Balmino, G.; Banerdt, W.B.; Head, J.W.; Johnson, C.L.; et al. Internal structure and early thermal evolution of mars from mars global surveyor topography and gravity. *Science* **2000**, *287*, 1788. [[CrossRef](#)] [[PubMed](#)]
93. Liu, K.F.; Mei, C.C. Slow spreading of a sheet of bingham fluid on an inclined plane. *J. Fluid Mech.* **1989**, *207*, 505–529. [[CrossRef](#)]
94. Nye, J.F. The mechanics of glacier flow. *J. Glaciol.* **1952**, *2*, 82–93. [[CrossRef](#)]
95. Hulme, G. The interpretation of lava flow morphology. *Geophys. J. R. Astron. Soc.* **1974**, *39*, 361–383. [[CrossRef](#)]
96. Coussot, P.; Piau, J.M. On the behavior of fine mud suspensions. *Rheol. Acta* **1994**, *33*, 175–184. [[CrossRef](#)]
97. Blake, S. Viscoplastic models of lava domes. In *Lava Flows and Domes: Emplacement Mechanisms and Hazard Implications*; Fink, J.H., Ed.; Springer: Berlin/Heidelberg, Germany, 1990; pp. 88–126.
98. Phipps, S.P. Rheology of serpentinite muds in the mariana-izu-bonin forearc. *Proc. Ocean Drill. Program Sci. Results* **1992**, *125*, 363–372. [[CrossRef](#)]
99. Rudolph, M.L.; Manga, M. Mud volcano response to the 4 April 2010 el mayor-cucapah earthquake. *J. Geophys. Res. Solid Earth* **2010**, *115*, B12211. [[CrossRef](#)]
100. Yusifov, M.; Rabinowitz, P.D. Classification of mud volcanoes in the south caspian basin, offshore Azerbaijan. *Mar. Pet. Geol.* **2004**, *21*, 965–975. [[CrossRef](#)]
101. O'Brien, J.S.; Julien, P.Y. Laboratory analysis of mudflow properties. *J. Hydraul. Eng.* **1988**, *114*, 877–887. [[CrossRef](#)]
102. Major, J.J.; Pierson, T.C. Debris flow rheology: Experimental analysis of fine-grained slurries. *Water Resour. Res.* **1992**, *28*, 841–857. [[CrossRef](#)]
103. Kopf, A.J. Significance of mud volcanism. *Rev. Geophys.* **2002**, *40*, 2-1–2-52. [[CrossRef](#)]
104. Rudolph, M.L.; Karlstrom, L.; Manga, M. A prediction of the longevity of the lusi mud eruption, Indonesia. *Earth Planet. Sci. Lett.* **2011**, *308*, 124–130. [[CrossRef](#)]
105. Smith, D.E.; Lerch, F.J.; Nerem, R.S.; Zuber, M.T.; Patel, G.B.; Fricke, S.K.; Lemoine, F.G. An improved gravity model for mars: Goddard mars model 1. *J. Geophys. Res. Planets* **2012**, *98*, 20871–20889. [[CrossRef](#)]
106. Konopliv, A.S.; Yoder, C.F.; Standish, E.M.; Yuan, D.-N.; Sjogren, W.L. A global solution for the mars static and seasonal gravity, mars orientation, phobos and deimos masses, and mars ephemeris. *Icarus* **2006**, *182*, 23–50. [[CrossRef](#)]

107. Ivanov, M.A.; Hiesinger, H.; Erkeling, G.; Hielscher, F.J.; Reiss, D. Major episodes of geologic history of isidis planitia on mars. *Icarus* **2012**, *218*, 24–46. [[CrossRef](#)]
108. Ghent, R.R.; Anderson, S.W.; Pithawala, T.M. The formation of small cones in isidis planitia, mars through mobilization of pyroclastic surge deposits. *Icarus* **2012**, *217*, 169–183. [[CrossRef](#)]
109. McGowan, E.M. The utopia/isidis overlap: Possible conduit for mud volcanism on mars. *Icarus* **2011**, *212*, 622–628. [[CrossRef](#)]
110. Davies, R.J.; Brumm, M.; Manga, M.; Rubiandini, R.; Swarbrick, R.; Tingay, M. The east java mud volcano (2006 to present): An earthquake or drilling trigger? *Earth Planet. Sci. Lett.* **2008**, *272*, 627–638. [[CrossRef](#)]
111. Pelletier, B.R. Review of surficial geology and engineering hazards in the Canadian offshore. *Atl. Geol.* **1979**, *15*, 55–91. [[CrossRef](#)]
112. Tsunogai, U.; Ishibashi, J.; Wakita, H.; Gamo, T.; Watanabe, K.; Kajimura, T.; Kanayama, S.; Sakai, H. Peculiar features of suiyo seamount hydrothermal fluids, izu-bonin arc: Differences from subaerial volcanism. *Earth Planet. Sci. Lett.* **1994**, *126*, 289–301. [[CrossRef](#)]
113. Pavlov, A.A.; Vasilyev, G.; Ostryakov, V.M.; Pavlov, A.K.; Mahaffy, P. Degradation of the organic molecules in the shallow subsurface of mars due to irradiation by cosmic rays. *Geophys. Res. Lett.* **2012**, *39*, L13202. [[CrossRef](#)]
114. Cleaves, H.J.; Miller, S.L. Oceanic protection of prebiotic organic compounds from UV radiation. *Proc. Natl. Acad. Sci. USA* **1998**, *95*, 7260–7263. [[CrossRef](#)] [[PubMed](#)]
115. Etiope, G.; Oehler, D.Z.; Allen, C.C. Methane emissions from earth's degassing: Implications for mars. *Planet. Space Sci.* **2011**, *59*, 182–195. [[CrossRef](#)]



© 2018 by the authors. Licensee MDPI, Basel, Switzerland. This article is an open access article distributed under the terms and conditions of the Creative Commons Attribution (CC BY) license (<http://creativecommons.org/licenses/by/4.0/>).